

Complex-Shaped Cellulose Composites Made by Wet Densification of 3D Printed Scaffolds

Michael K. Hausmann, Gilberto Siqueira,* Rafael Libanori,* Dimitri Kokkinis, Antonia Neels, Tanja Zimmermann, and André R. Studart*

Cellulose is an attractive material resource for the fabrication of sustainable functional products, but its processing into structures with complex architecture and high cellulose content remains challenging. Such limitation has prevented cellulose-based synthetic materials from reaching the level of structural control and mechanical properties observed in their biological counterparts, such as wood and plant tissues. To address this issue, a simple approach is reported to manufacture complex-shaped cellulose-based composites, in which the shaping capabilities of 3D printing technologies are combined with a wet densification process that increases the concentration of cellulose in the final printed material. Densification is achieved by exchanging the liquid of the wet printed material with a poor solvent mixture that induces attractive interactions between cellulose particles. The effect of the solvent mixture on the final cellulose concentration is rationalized using solubility parameters that quantify the attractive interparticle interactions. Using X-ray diffraction analysis and mechanical tests, 3D printed composites obtained through this process are shown to exhibit highly aligned microstructures and mechanical properties significantly higher than those obtained by earlier additively manufactured cellulose-based materials. These features enable the fabrication of cellulose-rich synthetic structures that more closely resemble the exquisite designs found in biological materials grown by plants in nature.

1. Introduction

Cellulose offers a sustainable natural resource for the manufacturing of a broad variety of materials in the form of thin films,^[1] emulsion stabilizers,^[2] membranes or foams for waste water management,^[3,4] food packaging and food additives,^[5] and reinforcements for composites.^[6,7] Whereas the extensive research on cellulose has made available a wide range of cellulose-based building blocks for many applications, current manufacturing technologies do not allow yet for full exploitation of their potential. This is evident by comparing the relatively simple structure of synthetic cellulose-based materials with the hierarchical architecture of biological materials made predominantly from cellulose, such as wood. Further advancements in manufacturing technologies are crucial to enable harnessing the potential of cellulose as a sustainable material resource for the future.

The wide availability of 3D printing technologies has recently given new impulse on the search for manufacturing approaches that offer greater control over the shape and structure of synthetic

materials.^[8–11] Using stereolithographic, inkjet, and laser- or extrusion-based processes, 3D printing provides shaping capabilities thus far inaccessible by other manufacturing processes.^[12–15] The control over the macroscopic shape inherent of these additive technologies have been combined with different approaches to structure the printed material at smaller length scales below the resolution of the printer. This is possible by designing inks or resins with building blocks that can assemble into controlled structures during or after printing. The assembly process can be directed by external forces, using for example light, magnetic fields, acoustic waves, or shear forces imposed by an extrusion nozzle.^[16–19] In recent examples, 3D printing of inks programmed to undergo directed assembly has allowed for the creation of self-shaping composites inspired by the morphology of seedpods and flowers.^[20,21] Alternatively, polymer objects with reinforcement architectures that resemble the hierarchical structure of wood have been 3D printed using self-assembling liquid crystalline building blocks.^[22]

M. K. Hausmann, Dr. G. Siqueira, Dr. T. Zimmermann
Empa
Swiss Federal Laboratories for Materials Science and Technology
Cellulose and Wood Materials Laboratory
8600 Dübendorf, Switzerland
E-mail: gilberto.siqueira@empa.ch

M. K. Hausmann, Dr. R. Libanori, Dr. D. Kokkinis, Prof. A. R. Studart
Complex Materials
Department of Materials
ETH Zürich
8093 Zürich, Switzerland
E-mail: rafael.libanori@mat.ethz.ch; andre.studart@mat.ethz.ch

Dr. A. Neels
Empa
Swiss Federal Laboratories for Materials Science and Technology
Center for X-ray Analytics
8600 Dübendorf, Switzerland

 The ORCID identification number(s) for the author(s) of this article can be found under <https://doi.org/10.1002/adfm.201904127>.

DOI: 10.1002/adfm.201904127

Although the shear-induced assembly of cellulose fibrils and nanocrystals in extrusion-based 3D printing has already been demonstrated,^[23–25] the concentration of cellulose that can be added to the inks remains very limited, typically below 6.6 vol% for unmodified cellulose nanocrystals (CNCs) dispersed in a polymer matrix and 1.3–2.6 vol% for cellulose nanofibers (CNFs) dispersed in water.^[26–31] Such diluted conditions are appropriate for the inkjet printing of cellulose micropatterns on flat substrates^[13] or the stereolithographic printing of liquid resins into CNC-laden complex geometries,^[14,32] but is not sufficient to create 3D objects with high cellulose content. 3D printed objects with high mechanical properties and volume fraction of cellulose acetate (35 wt%) have been recently reported, but the absence of filler particles in this system prevents the design of more elaborate bioinspired cellulose architectures.^[33] Other recent works have shown that inks with up to 30–40 wt% CNC can be printed into complex-shaped scaffolds and composites.^[24,34] However, these very high CNC concentrations lead to drying issues at the printing nozzle and to very high viscosity and yield stress levels that prevent the flow-induced alignment of cellulose nanocrystals at reasonable applied pressures.^[8,35] By contrast, the volume fraction of cellulose in biological materials like wood can reach levels as high as 40–50 wt%.^[7] Due to the low volume fraction achieved with current manufacturing processes, 3D printed objects cannot fully benefit from the attractive mechanical and functional properties of cellulose-based building blocks. Moreover, the use of cellulose as a sustainable material resource can only be fully justified if its concentration reaches a significant level in final cellulose-based products. This challenge becomes even more critical in view of the anisotropic nature of cellulose fibrils and nanocrystals, which reduces the maximum volume fraction of particles that can be used before the ink becomes too viscous.

Here, we report a simple approach to manufacture complex-shaped 3D printed polymer composites with volume fraction of nanocelluloses (CNC and CNF) that can be varied from about 13 vol% up to a thus far inaccessible level of 27.35 vol%. In this approach, the interactions between nanocellulose particles suspended in water are first tuned to achieve the rheological properties required for extrusion-based printing of distortion-free structures. After the printing process, the structure is densified by inducing attractive interactions between the cellulose nanoparticles upon exchange of water by a poor solvent. To illustrate this simple processing route and identify the parameters controlling the wet densification process, we study the effect of different solvent mixtures on the volume fraction of nanocelluloses in 3D printed objects. Next, X-ray diffraction experiments are performed to quantify the level of alignment of the cellulose nanoparticles after the printing and solvent exchange processes. The impact of the wet densification process on the mechanical properties of composites produced using this route is then investigated and compared to those of other cellulose-based 3D printed materials. Finally, the shaping freedom enabled by additive manufacturing is combined with the wet densification process to manufacture 3D printed demonstrators with unique geometrical complexity and load-bearing capacity.

2. Results and Discussion

2.1. Manufacturing of Complex-Shaped Composites

The manufacturing of complex-shaped composites with high nanocellulose concentrations is demonstrated using two main steps: a) 3D printing of a cellulose scaffold with highly aligned microstructure and b) wet densification of the printed scaffold through a solvent exchange process (Figure 1). The printing step requires the formulation of nanocellulose-based inks displaying rheological properties suitable for the direct ink writing (DIW) process. Previous works have shown that shear-thinning behavior, sufficient yield stress, a finite elastic modulus and fast elastic recovery are key rheological properties for the 3D printing of distortion-free structures by DIW.^[23,24] These properties can be potentially achieved if the ink contains particles that form a percolating attractive network under rest. Because the main goal was to maximize the cellulose concentration in the final printed scaffold, our ink was designed to contain the highest possible CNC content while still ensuring a shear-thinning behavior and sufficiently low viscosity for extrusion under moderate applied pressures. Shear thinning is favored in such inks due to the alignment of the CNC particles during the extrusion process (Figure 1A). In addition to this high CNC content, a small fraction of cellulose nanofibers (CNFs) was added to the formulation to increase the yield stress, storage modulus and elastic recovery of the ink (Section S1 and Figure S1, Supporting Information). Due to its very high aspect ratio in the order of 200, CNFs favor the formation of the desired percolating network of particles.^[7] Based on these considerations, a final ink containing 20 wt% CNC and 1 wt% CNF suspended in water was used for 3D printing of cellulose scaffolds. At this solid fraction of CNCs, the fast drying issues typically observed in highly concentrated inks are circumvented^[24,34] and the viscosity and yield stress of the ink are sufficiently low to enable the partial alignment of cellulose nanocrystals during extrusion.

2.2. Densification Process

Cellulose scaffolds were densified in a subsequent step by immersing the printed object into a solvent bath of selected composition (Figure 1B). Densification is achieved when the liquid in the bath is a poor solvent for the cellulose particles, leading to the development of attractive interparticle interactions (Section S2 and Figure S2, Supporting Information). Under such conditions, the average distance between the particles within the printed object reduces, leading to macroscopic shrinkage and densification. To assess the quality of the solvent with respect to the nanocellulose particles, we use Hansen solubility parameters previously reported in the literature (Figure 1C; Table S2, Supporting Information). According to Hansen, the total solubility parameter of a liquid (δ_T) is determined by three contributions: i) the hydrogen bonding component (δ_H), the polar component (δ_P), and the dispersive component (δ_D).^[36,37] Overall, a poor solvent is expected to exhibit Hansen solubility parameters that differ significantly from those of the suspended particles. Earlier work^[38–42] has

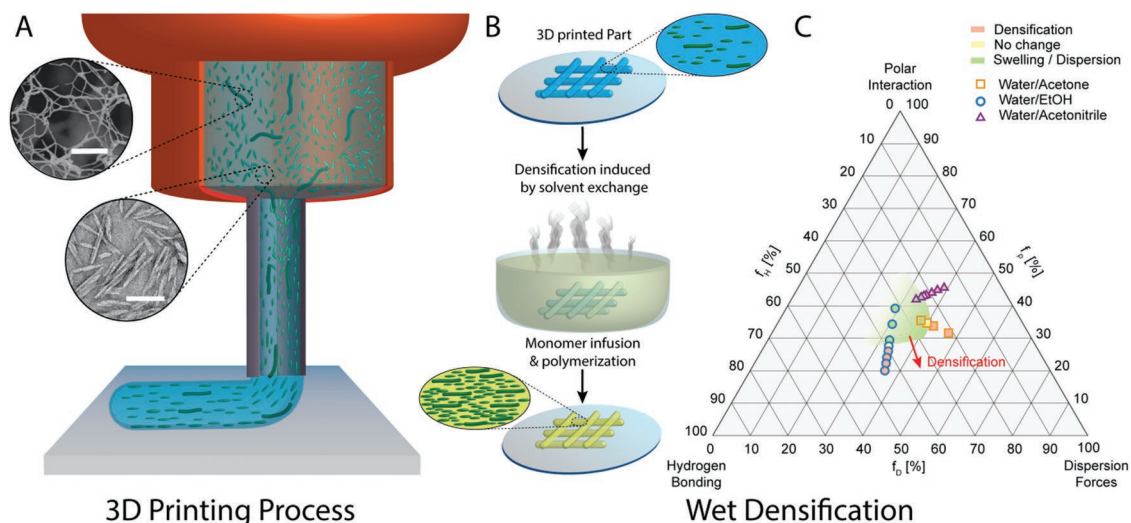


Figure 1. Illustration of the 3D printing and wet densification processes used to produce complex-shaped objects with high cellulose concentration. A) The alignment of cellulose nanofibers (CNF) and nanocrystals (CNC) during the flow of the ink within the extrusion nozzle. The insets show electron microscopy images of CNFs (top) and CNCs (bottom) obtained from diluted suspensions. Scale bar: 2 μm and 100 nm, respectively. B) Wet densification process induced by solvent exchange, followed by polymerization of infiltrated monomers initially present in the solvent bath. C) Ternary diagram indicating the relative weight of the solubility parameters of the solvent mixtures used for wet densification. The solubility parameters are presented in terms of relative fractions of hydrogen bonding interactions (f_H), dispersion forces (f_D), and polar interactions (f_P). The colors indicate the solvent mixtures that lead to swelling/dispersion, no dimensional changes, and wet densification of the printed objects.

shown that the range of solubility parameters for acid-hydrolyzed nanocellulose particles matches well the δ_H , δ_D , and δ_P values of water, which explains the good dispersibility of the as-hydrolyzed CNC/CNF particles in aqueous medium. To achieve the desired poor solvent condition required for scaffold densification, water-miscible solvents such as ethanol, acetone, and acetonitrile can be added to the initial aqueous phase (Figure 1C; Section S3 and Figures S3–S6, Supporting Information).

We investigate the effect of the solvent composition on the densification process by systematically changing the solubility parameters of the liquid mixture relative to that of cellulose. Our experiments indicate that the scaffold densifies continuously when immersed in an aqueous solution containing increasing concentrations of ethanol, acetone or acetonitrile in water (Figure 2A). Taking mixtures of water and ethanol as an example, we observe a change in solid volume fraction from 3.67 to 24.5 vol%, as the fraction of ethanol is increased from 65.5 to 100 vol%. This trend is in agreement with the qualitative description of the effect of solvents with distinct solubility parameters on the densification of cellulose-based membranes produced through spinning processes.^[43] Based on these data, it is possible to define an area in a solubility diagram that leads to dispersion or densification of the cellulose scaffold (green area in Figure 1C).

2.3. Cohesive Energy Density

To gain a better quantitative understanding of the physical processes that control the wet densification process, our results were interpreted in terms of the cohesive energy density (CED) of cellulose compared to that of the different solvent mixtures.

The CED corresponds to the increase in internal energy per unit volume of a substance if all intermolecular forces are removed.^[44–47] This parameter is therefore an indicator of the energy gained through attractive intermolecular interactions within a substance and can be determined from the total Hansen solubility parameters as follows:

$$\text{CED} = \delta_T^2 = \delta_H^2 + \delta_D^2 + \delta_P^2 \quad (1)$$

where δ_H , δ_D , and δ_P represent, respectively, the hydrogen bonding, and the polar and the dispersive contributions to the total solubility parameter.

For our CNC suspensions, liquid mixtures with CED values comparable to those of the suspended particles tend to be good solvents since the replacement of particle–particle interactions by particle–liquid interactions does not lead to a major net change in internal energy. By contrast, a mismatch between the CED values of the particles and of the liquid mixture will result in separation into particle-rich and liquid-rich phases. Because the estimated CED of hydrolyzed cellulose is comparable to that of water but higher than that of pure ethanol, acetone and acetonitrile (Figure 2B), the addition of these non-aqueous solvents into the liquid mixture will favor attractive interactions between the cellulose nanoparticles. Following this rationale, we take the mismatch in CED between particles and liquid mixture as an estimate of the reduction in internal energy of the wet scaffold achieved upon solvent exchange. This net change in CED can be physically interpreted as an internal stress that pulls particles together as a result of the increased attractive interactions between cellulose molecules. Taking such internal stress as the driving force of the wet densification process, one should expect the final relative density of the cellulose scaffolds to be proportional to the net change in CED after solvent exchange.

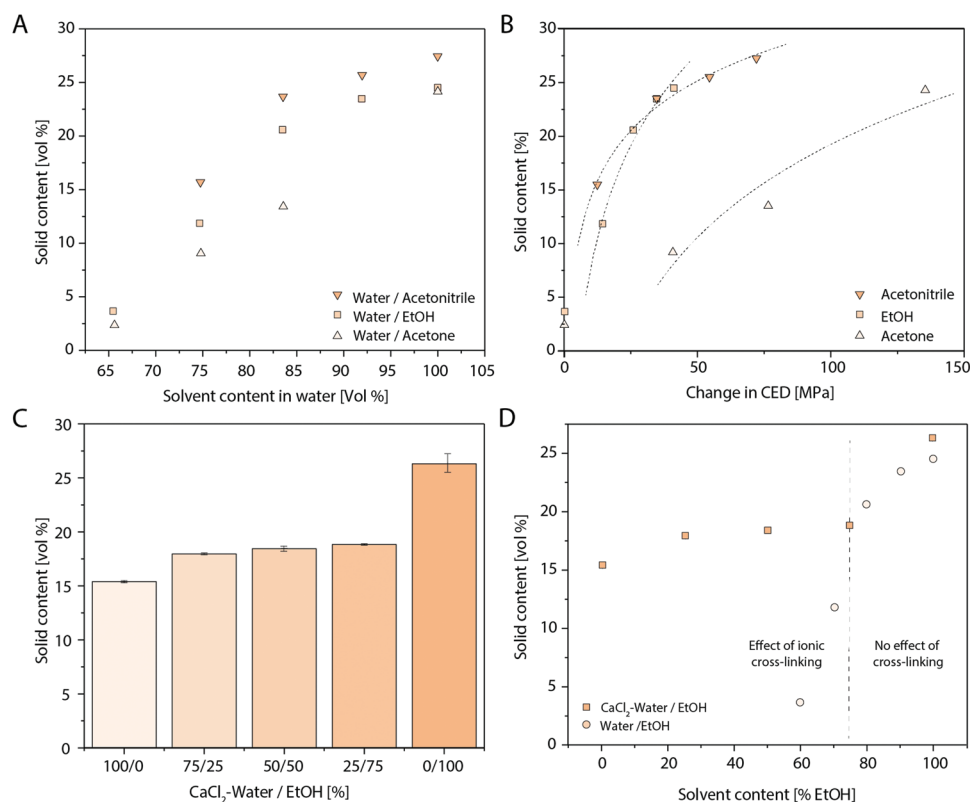


Figure 2. Solids content of cellulose scaffolds obtained via wet densification using solvent mixtures of different compositions. A) Solid content of the scaffold as a function of the concentration of acetonitrile, ethanol (EtOH) and acetone used in the aqueous solvent mixtures. B) Dependence of the solid content on the net change in CED induced by the solvent exchange process. The lines were obtained by fitting the data with a logarithmic function. C) Effect of the relative fraction between Ca-containing water (4 wt% CaCl_2) and ethanol on the solid content of scaffolds immersed in water/ethanol (EtOH) solutions. D) Comparison of the solids content achieved using water/EtOH solutions in the presence or the absence of 4 wt% CaCl_2 .

Indeed, our experimental data show that the solid content in the printed nanocellulose objects increase logarithmically with the net change in CED (Figure 2B). The obtained trend resembles the compaction behavior of powders in pressing operations, where a logarithmic dependence is also found between the relative density of the powder and the pressure applied onto the compact.^[48,49] Such analogy supports our physical interpretation that internal stresses induced by molecular interactions are at the origin of the wet densification process.

While the logarithmic dependence on the net CED change is observed for all the tested solvents, a stronger densification effect is achieved with ethanol and acetonitrile. To shed light on the possible causes of this difference, our physical picture of the densification process is complemented by a chemical description of the underlying molecular interactions (Figure 2B). From a chemical viewpoint, the development of internal stresses results from the replacement of the highly polar and hydrogen-bonding $-\text{OH}$ groups from the water molecules by solvent molecular moieties that display weaker interactions with the $-\text{OH}$ groups present on the surface of the cellulose particles. Because of their enhanced polar nature and hydrogen-bonding capability, the $-\text{OH}$ groups of water molecules interact more strongly with the cellulose surface, preventing the hydroxyl groups of CNCs/CNFs from establishing attractive molecular interactions between neighbor particles. This screening effect of the water molecules is attenuated by

replacing them with (excess) solvent molecules containing less polar and hydrogen-bonding functional groups. The less interacting solvent molecules are eventually displaced by direct attractive interactions between the $-\text{OH}$ groups on the cellulose surface, leading to the observed densification phenomenon. According to this interpretation, the excess of solvent molecules needed to remove water molecules from the cellulose surface will depend on their polar character and hydrogen-bonding ability. Based on the Hansen solubility parameters, we note that ethanol and acetonitrile show either polar or hydrogen-bonding values that come close to those of water (Section S3, Supporting Information). As a result, these two solvents can easily replace H_2O molecules from the cellulose surface and thus induce densification. By contrast, the polar and hydrogen-bonding Hansen parameters of acetone are both significantly lower compared to water. Consequently, a far greater excess of acetone is needed to remove water molecules from the cellulose surface and promote attractive interparticle interactions. Since the CED net change resulting from the solvent exchange with acetone still predicts densification to be more thermodynamically stable, we expect the shielding effect imposed by the water molecules to be only a kinetic constraint that can be overcome if enough time is provided for the densification process.

Besides the solvent quality, a cross-linker ion such as Ca^{2+} can also be used to increase the solid content of the printed cellulose object when the concentration of poor solvent (e.g. ethanol)

in the mixture is kept low. Due to their opposite charges, the Ca^{2+} ions and the hydrolyzed cellulose nanoparticles establish attractive electrostatic interactions that decrease the distance between nanocellulose particles, thus increasing the solid fraction of the object. To illustrate this effect, we evaluated the density of cellulose objects after introducing them in an immersion bath comprising a water–ethanol mixture with different concentrations of Ca^{2+} -containing aqueous phase. Cross-linking with Ca^{2+} leads to the formation of a percolating network of CNC/CNF particles that remains cohesive and gelled even in the absence of the poor solvent (ethanol). A CNC/CNF object immersed in an ethanol-free aqueous solution with 4 wt% CaCl_2 shows a solid content of 15.7 vol%, which is slightly higher than the initial CNC/CNF concentration of 14.6 vol% present in the initial ink. By contrast, immersion in a Ca-free aqueous solution without ethanol leads to complete disintegration of the object (Figure S5, Supporting Information). The cross-linking effect of Ca^{2+} can be combined with the solvent-induced densification effect through the addition of ethanol to the Ca^{2+} -containing aqueous solution used as immersion bath (Figure 2C). For ethanol concentrations higher than 70.4 vol% in the Ca^{2+} -containing bath, the solid fraction reaches values comparable to those obtained using Ca-free water–ethanol mixtures. At this point, the relative density of the object becomes dominated by the quality of the solvent (Figure 2C,D).

2.4. Composite and Mechanical Properties

3D printed nanocellulose objects subjected to wet densification can be further processed into composites containing very high concentrations of cellulose. Composites are generated here by introducing a polymer phase between the CNC/CNF particles using two different routes: supercritical drying of the wet printed material followed by infiltration of monomers or infiltration of the printed materials with a monomer in the wet state (Section S4 and Figures S7–S9 and S13, Supporting Information). The wet infiltration route is illustrated here as a means to obtain large nanocellulose-based composites without the need of costly equipment, which drastically simplifies the process as compared to the impregnation of supercritically dried scaffolds (Sections S2 and S4, Supporting Information). Advantages and limitations of these and other manufacturing routes used throughout this study are listed in Table S1 (Supporting Information). In this process, a mixture of monomer, cross-linker and photoinitiator is dissolved into the solvent bath used for the wet densification procedure. The presence of these components does not affect the wet densification step. As observed with the monomer-free mixtures, solvent exchange leads to a linear shrinkage of 40% relative to the initial printed dimensions. Because of its lower vapor pressure compared to ethanol, the monomer infiltrates the nanocellulose object during evaporation of the solvent. Following this approach, composites with nanocellulose concentrations of 27.35 vol% were generated by polymerizing the infiltrated monomer using UV light. The infiltration of the CNC/CNF scaffolds with the monomer enhances significantly the cohesion between filaments by forming a single continuous phase throughout the printed object (Figures S4–S8, Supporting Information). Additionally,

our experiments showed that the solvent exchange process can be carried without undesired shape distortion effects if the wall thickness of the 3D printed objects is smaller than approximately 5 mm. 3D scaffolds with thicker walls would require the use of solvents with a smaller CED mismatch to prevent differential shrinkage and distortion of the wall. For wall thicknesses equal or below 5 mm, we experimentally observed that the solvent exchange process takes less than 30 min. It is important to note that the shrinkage associated with the wet densification process should also be taken into account when designing the dimensions of the 3D printed object. Very recent work on cellulose-based structures subjected to solvent-induced shrinkage has shown that a compensation factor can be introduced in the design model to reach 3D objects with predictable final dimensions.^[50]

In addition to the high concentration of cellulose, 3D printing followed by wet densification also allows one to preserve the alignment of cellulose nanocrystals and nanofibers resulting from the DIW process and thus obtain 3D objects with deliberate CNC orientations. This feature enables the manufacturing of objects with aligned architectures inspired by wood and other biological materials (Figure 3A,B; see Sections S5–S7 in the Supporting Information). To explore this technology for the fabrication of bioinspired architectures it is crucial to quantify the level of alignment achieved during the 3D printing process and after infiltration of the densified scaffolds with monomers to generate the CNC-based composites. We quantified the level of nanocellulose alignment in single filaments and printed objects before and after infiltration using 2D wide-angle X-ray diffraction (Figure 3C–F). Printed objects were manufactured by depositing filaments next to each other so as to form a film, the height of which was twice the filament diameter. The X-ray data obtained for single filaments and printed objects show the expected strong alignment of the CNC/CNF particles along the printing direction. This is indicated by the two intensity peaks detected in the azimuthal X-ray scans (Figure 3C–F; Figures S10–S12 and Table S3, Supporting Information). The degree of alignment obtained in this study is comparable to that obtained in previous work using direct ink writing.^[24] The high nanocellulose particle orientation shown by the diffraction measurements was confirmed by scanning electron microscopy (SEM). Our SEM images show that the aligned CNC/CNF particles form a very dense microstructure that resembles the fibrillated architecture of the thickest and supporting cell wall layer S2 present in the secondary walls of plant cells.^[51] Infiltration of the nanocellulose filaments and printed films with the monomer result in less intense diffraction peaks, but does not alter the highly aligned nature of the structure (Figure 3C–F; Sections S5 and S6, Supporting Information). Because the chosen polymer phase exhibits similar refractive index to the cellulose nanoparticles, composites with remarkable optical transparency are obtained after infiltration and polymerization of the cellulose-based printed films (Figure 3G; Sections S7 and S8, Supporting Information). The high transparency achieved also results from the high chemical affinity between the monomer and the nanocelluloses, which is essential to promote wetting of the particles and prevent the formation of air pockets in the infiltrated structures.

Control over the alignment of CNCs/CNFs and the formation of strong interfaces between filaments and the polymer

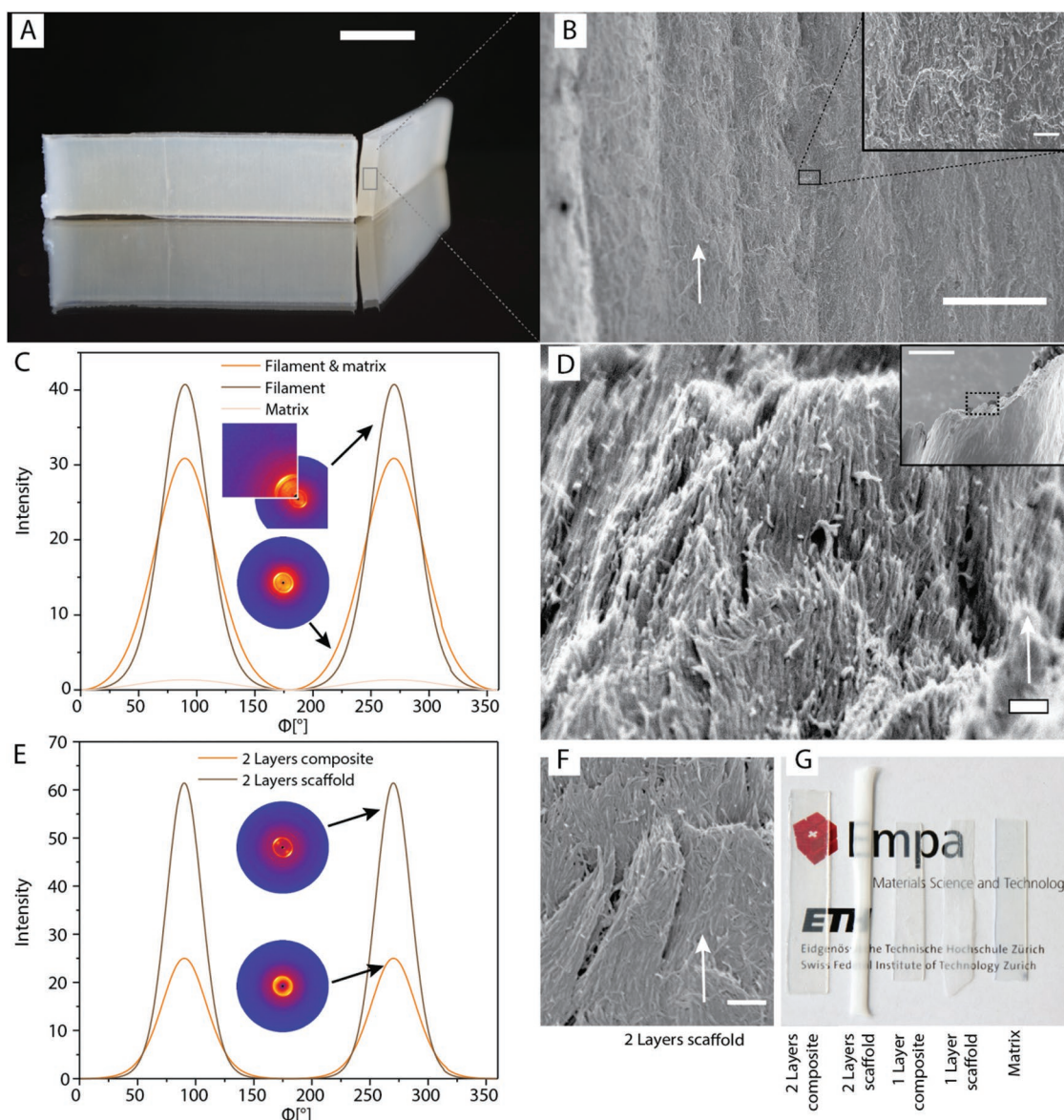


Figure 3. Structural characterization of cellulose-based filaments and printed objects before and after infiltration with a polymer matrix. A) 3D printed composite fabricated through the wet densification approach (scale bar: 1 cm), highlighting in the cross-section shown in (B) the good filament adhesion within the object. Scale bars: 200 μm in (B) and 10 μm in the inset of (B). The white arrow in (B) indicates one printed line. C) 2D-WAXS profiles of pure matrix, single scaffold filament and infiltrated scaffold filament. D) SEM image of single filament before infiltration showing high degree of alignment along the printing direction (white arrow). Scale bar: 200 nm. The inset shows the location of the imaged area within the filament (scale bar: 10 μm). E) 2D-WAXS profiles of two printed layers before (scaffold) and after infiltration with the polymer matrix (composite). F) SEM view of the two layer printed scaffold (scale bar: 400 nm). G) Optical transparency of pure polymer matrix, 3D printed dry scaffolds, and composite films with one and two layers.

matrix enables the fabrication of semitransparent cellulose-based 3D printed composites with tunable anisotropic mechanical properties (Figure 4; Figure S15, Supporting Information). To quantify the reinforcing effect of the CNC/CNF particles and the anisotropic properties of the resulting composites, we performed tensile and three-point bending tests in specimens exhibiting different particle orientations (Figure 4; Figures S16 and S17, Supporting Information). Composite samples were compared to the non-reinforced polymer matrix alone (cellulose-free) and to specimens obtained by simply drying the

CNC/CNF scaffolds in air. The mechanical results indicate that the polymer matrix is very soft and weak, with elastic modulus and tensile strength values of 1.6 and 7 MPa, respectively. Remarkably, the incorporation of 27.35 vol% of nanocellulose particles in this polymer matrix enhances the modulus and strength of the material by several orders of magnitude (Figure 4A–C). As expected, this is accompanied by a significant reduction of the ductility of the material. The major reinforcing effect imparted by the nanocellulose results from their high concentration in the composite and their intrinsically high

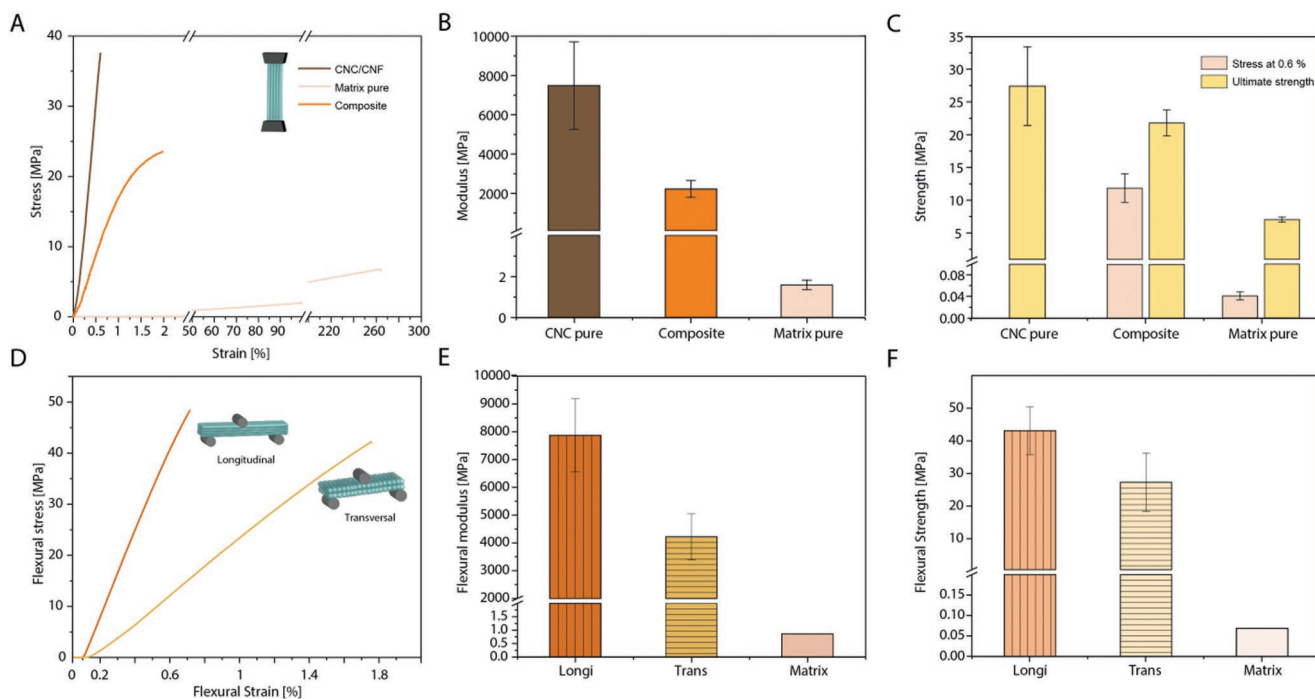


Figure 4. Mechanical performance of 3D printed composites obtained through the wet densification approach in tensile A–C) and flexural D–F) modes. A) Representative stress–strain curves obtained under tension for the matrix, 3D printed dry scaffold, and composite. B) Elastic modulus, C) strength at 0.6% deformation and maximum strength of the matrix, 3D printed dry scaffold, and composite. D) Representative stress–strain curves of the matrix and 3D printed composites in flexural mode. E) Flexural modulus and F) strength of the matrix and of composites tested in the longitudinal and transversal directions.

mechanical properties. Surprisingly, the CNC-based printed scaffolds alone show quite high mechanical properties, comparable to wood, even before infiltration and polymerization of the monomer (Figure 4A–C), which suggests that the wet densification process drastically increases the density of hydrogen bonds between cellulose particles in the printed object. Comparison of the mechanical properties of the composite with those of the pure nanocellulose specimen reveals that the concentration of CNC/CNF used in the composite is sufficient to harness the high modulus and strength of the cellulose particles alone while keeping some of the ductility associated with the polymer matrix (Figure 4A–C; Section S9, Supporting Information).

Flexural tests were conducted to study the effect of nanocellulose alignment and inter-filament adhesion on the mechanical properties of the composites. To this end, samples displaying different filament orientations with respect to the applied bending stresses were tested in a three-point bending setup (Figure 4D–F). The results show that composites with nanocellulose particles aligned parallel to the applied stresses (longitudinal configuration) reach a flexural modulus of 7.9 GPa, which is two-fold higher than that obtained when the specimens are tested in the perpendicular direction (transversal configuration). Despite the higher elastic modulus achieved in the longitudinal configuration, the strength of the composite was found to reach a comparable value of 40 MPa irrespective of the CNC alignment direction. The high flexural modulus and strength of composites tested transversely reflect the high adhesion between printed filaments and indicate that the nanocellulose particles are able to reinforce the polymer matrix even

when aligned perpendicular to the main stress direction. With the high concentration of CNC/CNF particles achieved through the wet densification process, the reinforcement effect achieved is significantly stronger than that observed in cellulose-based 3D printed composites previously reported in the literature (Figure 4D–F; Section S9, Supporting Information).^[24,34] The mechanical properties of the composites are expected to be further improved if the CNC particles are combined with stronger polymer matrices. Taking for example cellulose acetate as polymer matrix, it should be possible to generate strong and stiff 3D printed objects featuring complex shapes and an all-cellulose hierarchical architecture.^[33,52]

The high cellulose concentration and mechanical properties demonstrated using simple filaments and films were eventually translated to more complex 3D geometries by taking advantage of the intrinsic shaping freedom of extrusion-based 3D printed technologies. We demonstrate the geometrical design freedom accessible with our nanocellulose-based inks by first printing a complex-shaped jar exhibiting overhangs and asymmetric features (Figure 5A–D). After printing, the jar was subjected to wet densification, followed by wet monomer infiltration and light-induced polymerization. Notably, the fine geometrical features remain undistorted during the wet densification step, in spite of the large linear shrinkage of approximately 40% that occurs in this process. This high shrinkage led to a remarkable cellulose concentration of 27.35 vol% in the final composite. A hollow truncated cone and a honeycomb design were also 3D printed, as examples of lightweight structures that can be manufactured with our process. To illustrate the high stiffness and strength

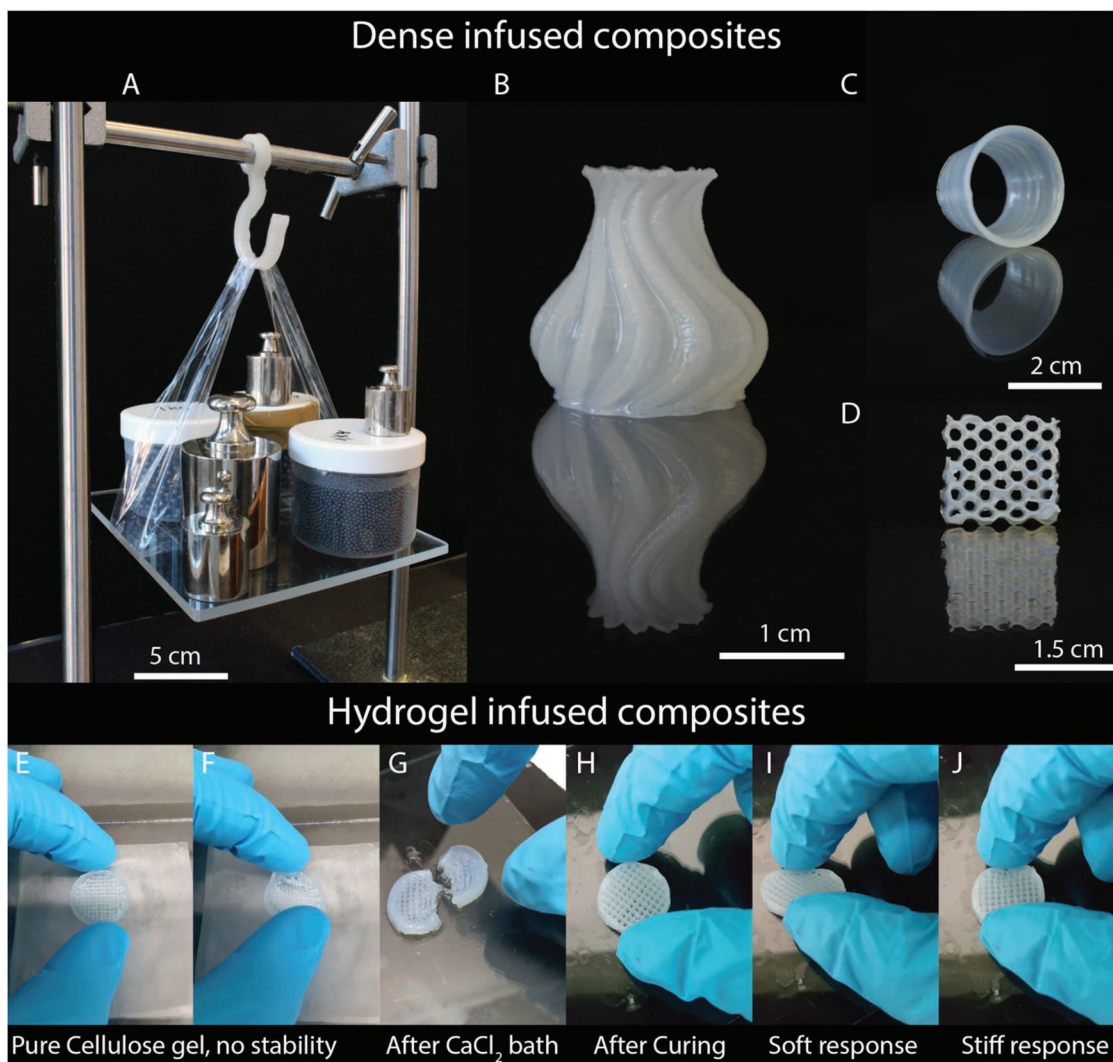


Figure 5. 3D printed functional parts with high volume fraction of cellulose (27.35 vol%). A) Printed hook (6.1 g) carrying a load of 4.5 kg. B) Printed jar with complex geometry. C,D) Printed truncated cone and honeycomb structures. E–J) Cellulose-based 3D printed composites prepared from hydrogels with lower cellulose concentration: E,F) hydrogel with no mechanical stability obtained right after printing and G) hydrogel after one day in bath of CaCl_2 solution, showing improved stiffness but low strength, and H–J) composite obtained after infiltration of hydrogel with monomer and UV curing. The infiltrated composite shows stiff response when compressed along the strut direction and elastic deformation when tested at an angle of 45° relative to the strut axis (see Videos S1–S4 in the Supporting Information).

of the final printed objects, we fabricated a hook that can bear a load that is 737 times higher than its own weight without significant extension or rupture (Figure 5A). The mechanical properties can be further controlled by infiltrating the printed scaffolds with different polymer matrices (Section S10 and Figure S18, Supporting Information).

2.5. A Versatile Approach

While a high concentration of nanocellulose particles is required to print stiff and load-bearing structures, the use of inks with lower cellulose contents that can be cross-linked with Ca^{2+} ions and swollen in water offer the possibility to produce soft hydrogels exhibiting tailored macroscopic geometries and

mechanical response. This was demonstrated by immersing an as-printed grid-like structure into a Ca-containing aqueous solution loaded with monomers, followed by light-induced polymerization of the monomer to create a soft composite with squared cellular architecture. The lateral compliance of the final structure depends on the angle at which it is mechanically loaded. Loading along the struts lead to stiff response, whereas a more compliant behavior is observed when the mechanical load is applied at an angle of 45° with respect to the strut axis (Figure 5E–J). The possibility to tailor the mechanical response of such structures by tuning the nanocellulose concentration in the precursor hydrogel and the cellular architecture of the printed object opens a large parameter space for the design of biocompatible cellulose-based gels and composites for biomedical and functional applications.

3. Conclusions

Complex-shaped composites with cellulose concentration up to 27.35 vol% can be created through the wet densification of 3D printed scaffolds. The densification process involves the exchange of the aqueous phase of the printed wet scaffold by a liquid mixture that works as a poor solvent for the cellulose particles. The poor solvent characteristics of the liquid mixture can be quantified using Hansen solubility parameters, which provide a measure of the cohesive energy density (CED) of the solvent mixture. Liquids with CED comparable to that of cellulose will work as good solvents, enabling the dispersion of a high concentration of cellulose particles in the ink used for 3D printing. By contrast, solvents with significantly different CED values will exhibit poor dispersion capabilities and induce attractive interactions between the cellulose particles within the 3D printed scaffolds. The increase in scaffold density during wet densification was found to be directly proportional to the change in CED resulting from the solvent exchange process. This quantitative relationship offers a sound physical interpretation of the wet densification phenomenon and provides guidelines for the selection of solvent mixtures that can effectively increase the cellulose content of 3D printed scaffolds. Because of their high cellulose concentration, composites obtained via infiltration of wet densified scaffolds with an organic phase show significantly higher fracture strength and stiffness compared to state-of-the-art 3D printed cellulose-based materials. This strengthening effect arises from the very high concentration of cellulose achieved in the final composite and is also partly affected by the strong alignment of the cellulose particles along the extrusion direction during the printing process. Such alignment can be combined with the shaping freedom enabled by 3D printing and the flexibility in materials choice offered by the densification and infiltration procedures to manufacture complex-shaped objects with unprecedentedly high mechanical properties and volume fraction of cellulose. The high level of structural complexity and control achieved with this combined process opens the way to the fabrication of cellulose-based materials that capture some of the design principles of biological structures like wood and morphing plant structures. Since mechanical stability and high cellulose content are key to achieve long-term durability and to fully benefit from the sustainable nature of this material resource, the proposed manufacturing workflow is also expected to have a major impact in future cellulose-based structural, biomedical and energy-related products.

4. Experimental Section

Materials: 2-Hydroxyethyl methacrylate (HEMA) (98%), *N*-isopropylacrylamide (NIPAM), and *N,N'*-methylenebis(acrylamide) (MBA) were purchased from Sigma-Aldrich. The functional PUA oligomers (BR3741A) and BR571) and the photoinitiator bis(2,4,6-trimethylbenzoyl)-phenylphosphineoxide (Irgacure 819) were generously provided by Dymax and BASF, respectively. Calcium chloride powder (CaCl₂) was purchased from Merck. Cellulose nanocrystals (CNCs) were prepared via sulfuric acid hydrolysis of eucalyptus pulp according to a published procedure^[53] and were purchased from the USDA Forest Service–Forest Products Laboratory (Madison, WI). Never-dried

elemental chlorine free (ECF) cellulose fibers from bleached softwood pulp (*Picea abies* and *Pinus* spp.) were obtained from Stendal GmbH (Berlin, Germany) and used for the production of cellulose nanofibers (CNFs). Transmission electron microscopy (TEM) images of CNCs and CNFs used in the study are shown in Figures S19 and S20 (Supporting Information). 2,2,6,6-Tetramethyl-1-piperidinyloxy (TEMPO) and sodium hypochlorite (NaClO) solutions (12–14% chlorine) were purchased from VWR International. Sodium bromide (NaBr ≥ 99%) and sodium hydroxide (NaOH ≥ 99%) were obtained from Sigma-Aldrich (Buchs, Switzerland).

Preparation and Characterization of Inks—Cellulose-Based Inks: TEMPO-CNFs were produced according to a well-established protocol from Saito et al.,^[54] which is extensively described elsewhere.^[55] Freeze-dried CNCs (0.98 wt% sulfur content; Figure S19, Supporting Information) and never-dried TEMPO-CNFs in water (CNF concentration of 1.33 wt% relative to water; Figure S20, Supporting Information) were mixed for 5 min at 2500 and 3500 rpm, respectively, in a speed mixer (model DAC 150.1 FVZ). The resulting gel contained 20 wt% CNC and 1 wt% CNF. This cellulose-based gel was left for swelling for one night, mixed at 3500 rpm for 5 min and stored in the fridge prior to testing. Before further processing and printing, the gel was filled in plastic cartridges and centrifuged for 10 min at 3500 rpm to remove bubbles.

Preparation and Characterization of Inks—Rheology of Inks: The rheological characterization of the inks was performed using an MCR 302 rheometer from Anton Paar. Measurements were carried out using a plate-plate geometry with 50 mm diameter and a gap of 0.5 mm at a constant temperature of 20 °C. Shear rate sweeps were performed at shear rates ranging from 0.001 to 1000 s⁻¹ at logarithmically spaced intervals with four points per decade. Amplitude sweeps were performed from 0.1 to 1000% using similar logarithmic intervals at a frequency of 1 Hz. The yield stress of the inks was determined by applying an increasing shear stress from 1 to 1000 Pa and measuring the deformation response. The stress corresponding to the change in slope in the shear stress versus deformation curves was taken as the yield stress of the ink.

Preparation and Characterization of Composites—3D Printing: Cellulose scaffolds were printed using a direct ink writer (DIW) from EnvisionTEC (Bioplotter Manufacturing series). The gels were filled in plastic cartridges and extruded through uniform steel needles with compressed air at pressures in the range 2.1–2.4 bar and at a fixed temperature of 20 °C. The extrusion needles were 27 mm long and exhibited a non-tapered geometry with diameter of 0.41 mm.

Preparation and Characterization of Composites—Freeze-Drying: Freeze-dried scaffolds were prepared by plunging printed gel structures into liquid nitrogen and placing the sample in the freeze-dryer (SRK System Technik GmbH–LYOVAC) for removal of the aqueous phase. Freeze-drying was accomplished by changing the temperature and pressure in the chamber so as to directly sublimate the ice.

Preparation and Characterization of Composites—Supercritical Drying: Some of the scaffolds were dried under supercritical conditions. Prior to supercritical drying, the water-based gel was plunged into an ethanol bath. The ethanol was changed several times to make sure most of the water is eliminated. Supercritical drying was conducted in a dedicated equipment (Quorum Technologies–Polaron), where the ethanol is first replaced by liquid CO₂ before removal of the liquid phase under supercritical conditions (37 °C, 100 bar).

Preparation and Characterization of Composites—Resin Formulation: The resin used as polymer matrix of the composite is a mixture of HEMA/BR-3741 A/Irgacure 819 at weight fractions of 50, 49.5, and 0.5 wt%, respectively. The resin was diluted with the solvent for the infiltration step. When pure ethanol was used as solvent, a solvent:resin weight ratio of 2:1 was utilized. The resin:water ratio for the hydrogels was adjusted to achieve the targeted final water content desired for the gel.

Preparation and Characterization of Composites—Infiltration of Supercritically Dried Scaffolds: Supercritically dried samples were plunged into a liquid bath of HEMA and isostatically pressed at 5000 bar for 5 min prior to a one week vacuum infiltration process. After infiltration, the samples were UV cured for 10 min on both sides under continuous nitrogen (N₂) flow to avoid oxygen inhibition of the polymer reaction.

Preparation and Characterization of Composites—Infiltration of Wet Scaffolds: Some of the scaffolds were directly infiltrated with monomer while still in the wet state. In this case, the aqueous phase of the printed scaffolds was first solvent exchanged with ethanol to enable wet densification. After water removal, the ethanol bath was either replaced by an ethanol solution of HEMA (2:1 weight ratio of ethanol:HEMA/BR). The samples were kept in the bath under vacuum for 1 week to allow for infiltration of the resin and complete elimination of the ethanol. Infiltrated scaffolds were UV-cured for 10 min on both sides under continuous nitrogen (N_2) flow. The possibility to directly infiltrate the wet scaffolds in a pure HEMA/BR resin bath is also explored, which is also feasible. The concentration of cellulose nanocrystals in the final composites was estimated using Archimedes and geometrical methods (Section S12, Supporting Information).

Mechanical and Structural Characterization of Composites—Three-Point-Bending Measurements: 3D printed samples for three-point-bending measurements were produced according to the standard ISO D790-03.^[56] Tests were conducted in an universal mechanical testing machine (Shimadzu AGS-X, Japan) equipped with a 1 kN load cell. Samples were tested using a span width of 40 mm and a displacement rate of 1 mm min^{-1} .

Mechanical and Structural Characterization of Composites—Tensile Tests: 3D printed single- and double-layered films were printed and tested in tensile mode using an uniaxial Mechanical tester (Zwick Roell) with a load cell of 500 N. Measurements were performed in $12 \text{ mm} \times 2 \text{ mm}$ dog bone samples that were punched out from printed sheets (single and double layers). Stress data were recorded while applying a displacement rate of 5 mm min^{-1} . Strain was measured based on cross-head motion. Pure CNC/CNF dog-bone-shaped samples were obtained by stamping out films that were wet-densified films via solvent exchange and dried in air. Dog-bone-shaped specimens of CNC/CNF composites were prepared from UV-cured composite films generated through the wet densification and infiltration processes.

Mechanical and Structural Characterization of Composites—Dynamic Mechanical Analysis (DMA): Single and double layered films were printed and cut for DMA analysis (TA RSAIII). Cut samples were 5 mm wide, 40 mm long, and 0.35 mm thick. Tests were conducted using a span of 35 mm. Samples were measured with a frequency of 1 Hz while heated from -100 to $100 \text{ }^\circ\text{C}$ at a rate of $2 \text{ }^\circ\text{C min}^{-1}$ and a prestrain of 0.04%.

Mechanical and Structural Characterization of Composites—Differential Scanning Calorimetry (DSC): DSC measurements were performed at heating and cooling rates of $20 \text{ }^\circ\text{C min}^{-1}$ (DSC7 and DSC8000, Perkin Elmer). The experimental run consisted of a heating cycle from -90 to $60 \text{ }^\circ\text{C}$, followed by a ramp-down to $-90 \text{ }^\circ\text{C}$ and a holding time of 5 min at $-90 \text{ }^\circ\text{C}$ before a final heating to $60 \text{ }^\circ\text{C}$.

Mechanical and Structural Characterization of Composites—UV-Vis Spectroscopy: Light transmittance of 3D printed films was measured on a Shimadzu UV-3600 at wavelengths ranging from 300 to 1500 nm. The single- and double-layered samples used in these measurements had a thickness of around 0.32 and 0.6 mm, respectively.

Mechanical and Structural Characterization of Composites—Transmission Electron Microscopy (TEM): Cellulose nanocrystals were characterized by transmission electron microscopy (TEM, Jeol JEM-2200FS, USA, Inc.) using an acceleration voltage of 200 kV. Plasma activated (30 s) carbon-coated grids were used as a support onto which a 0.02 wt% suspension of the cellulose nanocrystals was deposited and stained with a 2 wt% solution of uranyl acetate for 30 s. The average lengths and diameters of the CNCs were measured with the software Image J.

Mechanical and Structural Characterization of Composites—Scanning Electron Microscopy (SEM): Scanning electron microscopy (SEM) was performed on an LEO 1530 using an accelerating voltage of 2 kV and a working distance of 5 mm. Sample cross-sections prior and after resin infiltration or mechanical testing were imaged. Before imaging, the samples were either glued with carbon adhesive tape onto aluminum sample holders or held with screw fastening systems. Samples were coated for 30 s at a current of 40 mA, a pressure of 0.8 Pa, and a working distance of 5 cm with tungsten to avoid surface charging.

Mechanical and Structural Characterization of Composites—Optical Microscopy (OM): All optical microscopy analyses were performed on an Axioplan microscope from Zeiss equipped with cross-polarized filters.

Mechanical and Structural Characterization of Composites—Wide-Angle X-Ray Diffraction (WAXD): 2D wide-angle X-ray diffraction (2D-WAXD; STOE IPDS-II, 0.71073 Mo $K\alpha$ radiation source) was used to study the degree of CNC alignment within the printed filaments and films. The equipment was operated at 40 mA and 50 kV for 30 min using a beam diameter of 0.5 mm in transmission mode. The samples were fixed on the goniometer head and then placed perpendicular to the beam to allow the X-rays to pass only through the specimen. The 2D-WAXD patterns were recorded on an Image Plate Detector System with a 340 mm diameter placed at a distance of 200 mm from the sample. For each sample position a full image was recorded covering a 2θ range from 3° to 40° . Azimuthal scans were integrated for the cellulose (200) reflection. Curves shown in Figure 3 have been obtained after subtraction of the background noise to the original curve.

Supporting Information

Supporting Information is available from the Wiley Online Library or from the author.

Acknowledgements

The authors thank B. Fisher for the DSC analysis, A. Huch for the TEM imaging, and C. Affolter and B. Weisse for allowing to use the mechanical testing equipment as well as Romain Carron for the help with UV Spectroscopy and Dr. Etienne Jeoffroy for the scientific discussions. A.R.S. greatly acknowledge the financial support from the Swiss National Science Foundation (Consolidator Grant number BSCG10_157696). A.R.S. and R.L. are thankful for the financial support from the Swiss Competence Center for Energy Research SCCER Mobility and the Swiss Innovation Agency Innosuisse. M.K.H. and G.D.S. greatly acknowledge the financial support from the Swiss National Science Foundation (200021_159906/1). This work also benefited from support of the Swiss National Science Foundation through the National Center of Competence in Research Bio-Inspired Materials. Reference 41 in the main manuscript and reference 3 in the supporting information file were corrected on January 23, 2020, after initial online publication.

Conflict of Interest

The authors declare no conflict of interest.

Author Contributions

Experiments were designed by A.R.S., G.S., R.L., T.Z., and M.H., and were conducted by M.H. The X-ray analysis was performed by A.N., and the polymer system was previously developed by D.K. SEM imaging was conducted by D.K. and M.H. The main paper and the Supporting Information were cowritten by A.R.S., G.S., R.L., and M.H. All authors discussed the results, the conclusions, and revised the manuscript at all stages.

Keywords

3D printing, alignment, cellulose nanocrystals, cellulose nanofibers, densification, solvent mixture

Received: May 23, 2019
Revised: November 3, 2019
Published online: December 9, 2019

- [1] M. Nogi, S. Iwamoto, A. N. Nakagaito, H. Yano, *Adv. Mater.* **2009**, 21, 1595.
- [2] J. O. Zoppe, R. A. Venditti, O. J. Rojas, *J. Colloid. Interface Sci.* **2012**, 369, 202.
- [3] R. H. Kollarigowda, S. Abraham, C. D. Montemagno, *ACS Appl. Mater. Interfaces* **2017**, 9, 29812.
- [4] Z. Zhang, G. Sèbe, D. Rentsch, T. Zimmermann, P. Tingaut, *Chem. Mater.* **2014**, 26, 2659.
- [5] H. Lee, J. Sundaram, S. Mani, in *Production of Cellulose Nanofibrils and Their Application to Food: A Review* (Eds: R. Prasad, V. Kumar, M. Kumar), Springer, Singapore **2017**, p. 1.
- [6] R. J. Moon, A. Martini, J. Nairn, J. Simonsen, J. Youngblood, *Chem. Soc. Rev.* **2011**, 40, 3941.
- [7] A. Dufresne, *Nanocellulose from Nature to High Performance Materials*, Walter de Gruyter GmbH, Berlin **2012**.
- [8] J. A. Lewis, *Adv. Funct. Mater.* **2006**, 16, 2193.
- [9] A. R. Studart, *Chem. Soc. Rev.* **2016**, 45, 359.
- [10] L. Dai, T. Cheng, C. Duan, W. Zhao, W. Zhang, X. Zou, J. Aspler, Y. Ni, *Carbohydr. Polym.* **2019**, 203, 71.
- [11] D. Chimene, K. K. Lennox, R. R. Kaunas, A. K. Gaharwar, *Ann. Biomed. Eng.* **2016**, 44, 2090.
- [12] S. Kumar, M. Hofmann, B. Steinmann, E. J. Foster, C. Weder, *ACS Appl. Mater. Interfaces* **2012**, 4, 5399.
- [13] R. Maren, N. Fernando, *Deposition of Cellulose Nanocrystals by Inkjet Printing*, American Chemical Society, Washington, DC **2009**, p. 157.
- [14] N. B. Palaganas, J. D. Mangadlao, A. C. C. de Leon, J. O. Palaganas, K. D. Pangilinan, Y. J. Lee, R. C. Advincula, *ACS Appl. Mater. Interfaces* **2017**, 9, 34314.
- [15] J. Suwanprateeb, *Polym. Int.* **2006**, 55, 57.
- [16] D. Kokkinis, M. Schaffner, A. R. Studart, *Nat. Commun.* **2015**, 6, 8643.
- [17] C. Minas, D. Carnelli, E. Tervoort, A. R. Studart, *Adv. Mater.* **2016**, 28, 9993.
- [18] R. R. Collino, T. R. Ray, L. M. Friedrich, J. D. Cornell, C. D. Meinhart, M. R. Begley, *Mater. Res. Lett.* **2018**, 6, 191.
- [19] T. Kim, R. Trangkanukulij, W. S. Kim, *Sci. Rep.* **2018**, 8, 3805.
- [20] A. Sydney Gladman, E. A. Matsumoto, R. G. Nuzzo, L. Mahadevan, J. A. Lewis, *Nat. Mater.* **2016**, 53, 413.
- [21] S. Miao, N. Castro, M. Nowicki, L. Xia, H. Cui, X. Zhou, W. Zhu, S.-j. Lee, K. Sarkar, G. Vozzi, Y. Tabata, J. Fisher, L. G. Zhang, *Mater. Today* **2017**, 20, 577.
- [22] S. Gantenbein, K. Masania, W. Woigk, J. P. W. Sesse, T. A. Tervoort, A. R. Studart, *Nature* **2018**, 561, 226.
- [23] M. K. Hausmann, P. A. Rùhs, G. Siqueira, J. Lauger, R. Libanori, T. Zimmermann, A. R. Studart, *ACS Nano* **2018**, 12, 6926.
- [24] G. Siqueira, D. Kokkinis, R. Libanori, M. K. Hausmann, A. S. Gladman, A. Neels, P. Tingaut, T. Zimmermann, J. A. Lewis, A. R. Studart, *Adv. Funct. Mater.* **2017**, 27, 1604619.
- [25] K. M. O. Håkansson, A. B. Fall, F. Lundell, S. Yu, C. Krywka, S. V. Roth, G. Santoro, M. Kvick, L. Prahl Wittberg, L. Wagberg, L. D. Soderberg, *Nat. Commun.* **2014**, 5, 4018.
- [26] H. Martınez vila, S. Schwarz, N. Rotter, P. Gatenholm, *Bioprinting* **2016**, 1–2, 22.
- [27] A. Rees, L. C. Powell, G. Chinga-Carrasco, D. T. Gethin, K. Syverud, K. E. Hill, D. W. Thomas, *BioMed Res. Int.* **2015**, 2015, 925757.
- [28] J. Leppiniemi, P. Lahtinen, A. Paajanen, R. Mahlberg, S. Metsa-Kortelainen, T. Pinomaa, H. Pajari, I. Vikholm-Lundin, P. Pursula, V. P. Hytonen, *ACS Appl. Mater. Interfaces* **2017**, 9, 21959.
- [29] V. C. F. Li, A. Mulyadi, C. K. Dunn, Y. Deng, H. J. Qi, *ACS Sustainable Chem. Eng.* **2018**, 6, 2011.
- [30] K. M. O. Håkansson, I. C. Henriksson, C. de la Pena Vazquez, V. Kuzmenko, K. Markstedt, P. Enoksson, P. Gatenholm, *Adv. Mater. Technol.* **2016**, 1, 1600096.
- [31] K. Markstedt, A. Mantas, I. Tournier, H. Martınez vila, D. Hagg, P. Gatenholm, *Biomacromolecules* **2015**, 16, 1489.
- [32] V. C.-F. Li, X. Kuang, A. Mulyadi, C. M. Hamel, Y. Deng, H. J. Qi, *Cellulose* **2019**, 26, 3973.
- [33] S. W. Pattinson, A. J. Hart, *Adv. Mater. Technol.* **2017**, 2, 1600084.
- [34] V. C.-F. Li, C. K. Dunn, Z. Zhang, Y. Deng, H. J. Qi, *Sci. Rep.* **2017**, 7, 8018.
- [35] B. G. Compton, J. A. Lewis, *Adv. Mater.* **2014**, 26, 5930.
- [36] C. M. Hansen, *Hansen Solubility Parameters: A User's Handbook*, 2nd ed., CRC Press, Inc., Boca Raton, FL **2007**.
- [37] C. M. Hansen, *Doctoral Dissertation: The Three Dimensional Solubility Parameter and Solvent Diffusion Coefficient*, Danish Technical Press, Copenhagen **1967**.
- [38] M. S. Reid, M. Villalobos, E. D. Cranston, *Nanoscale* **2016**, 8, 12247.
- [39] S. X. Peng, H. Chang, S. Kumar, R. J. Moon, J. P. Youngblood, *Cellulose* **2016**, 23, 1825.
- [40] S. Gardebjer, M. Andersson, J. Engstrom, P. Restorp, M. Persson, A. Larsson, *Polym. Chem.* **2016**, 7, 1756.
- [41] C. Bruel, Q. Beuguel, J. R. Tavares, P. J. Carreau, M. C. Heuzey, *J-FOR* **2018**, 7, 13.
- [42] Y. Yoo, J. P. Youngblood, *ACS Sustainable Chem. Eng.* **2016**, 4, 3927.
- [43] X. Jie, Y. Cao, J.-J. Qin, J. Liu, Q. Yuan, *J. Membr. Sci.* **2005**, 246, 157.
- [44] A. M. Kolker, V. P. Korolev, D. V. Batov, *J. Struct. Chem.* **2005**, 46, 927.
- [45] C. Bruel, J. R. Tavares, P. J. Carreau, M.-C. Heuzey, *Carbohydr. Polym.* **2019**, 205, 184.
- [46] Y. Marcus, *Phys. Chem. Liq.* **2017**, 55, 522.
- [47] M. Dack, *Aust. J. Chem.* **1975**, 28, 1643.
- [48] R. Heckel, *Trans. Metall. Soc. AIME* **1961**, 221, 671.
- [49] R. Panelli, F. Ambrozio Filho, *Powder Metall.* **1998**, 41, 131.
- [50] C. Thibaut, A. Denneulin, S. Rolland du Roscoat, D. Beneventi, L. Orgas, D. Chaussy, *Carbohydr. Polym.* **2019**, 212, 119.
- [51] Y. Zeng, M. E. Himmel, S.-Y. Ding, *Biotechnol. Biofuels* **2017**, 10, 263.
- [52] S. Chen, G. Schueneman, R. B. Pipes, J. Youngblood, R. J. Moon, *Biomacromolecules* **2014**, 15, 3827.
- [53] S. Beck-Candanedo, M. Roman, D. G. Gray, *Biomacromolecules* **2005**, 6, 1048.
- [54] T. Saito, A. Isogai, *Biomacromolecules* **2004**, 5, 1983.
- [55] R. Weishaupt, G. Siqueira, M. Schubert, P. Tingaut, K. Maniura-Weber, T. Zimmermann, L. Thony-Meyer, G. Faccio, J. Ihssen, *Biomacromolecules* **2015**, 16, 3640.
- [56] Standard Test Methods for Flexural Properties of Unreinforced and Reinforced Plastics and Electrical Insulating Materials, https://compass.astm.org/EDIT/html_annot.cgi?D790+17, (accessed: July 2019).